IEEE Access
Multidisciplinary | Rapid Review | Open Access Journal

Received March 16, 2022, accepted April 19, 2022, date of publication April 22, 2022, date of current version May 6, 2022.

Digital Object Identifier 10.1109/ACCESS.2022.3169783

Optimization of the Heat Dissipation Structure for Lithium-Ion Battery Packs Based on Thermodynamic Analyses

YAN LI, HONGHAI LIU, AND MIN YE, (Member, IEEE)
National Engineering Laboratory for Highway Maintenance Equipment, Chang'an University, Xi'an 710064, China

Corresponding author: Min Ye (mingye@chd.edu.cn)

This work was supported in part by the Science and Technology Innovation Team of Shaanxi Province under Grant 2020TD0012, and in part by the Innovative Talents Promotion Project of Shaanxi Province under Grant 2020KJXX-044.

ABSTRACT The battery thermal management system plays an important role in electric vehicles, and determines the performance and the lifespan of electric vehicles. In this paper, optimization of the heat dissipation structure of lithium-ion battery pack is investigated based on thermodynamic analyses to optimize discharge performance and ensure lithium-ion battery pack safety. First, the heat generation and heat transfer model of the lithium-ion battery cell are derived based on thermodynamic theory. Then, the thermodynamic governing equations of battery are established based on Fluent, and the model is verified by comparing simulation data and experimental data. Afterwards, the simulation model of pure electric vehicles and the model of the heat generation rate are established using ADVISOR to analyze the dynamic performance of the battery pack. Finally, the air-cooling structure of the battery pack is designed according to the temperature field distribution obtained from the Fluent simulation, which is optimized using a back propagation neural network combined with genetic algorithms for the air flow rate, air flow channel spacing between cells, and air inlet angle. Based on the results of the optimized structure, the optimized structure effectively increases the heat dissipation performance and eliminates temperature inconsistency between the cells.

INDEX TERMS Air cooling, thermodynamic analysis, heat dissipation structure optimization, battery thermal management system (BTMS).

I. INTRODUCTION

With the increasing scarcity of energy and the pollution created by fuel-powered cars, electric vehicles (EVs) have achieved a larger market share in recent years, and relevant policy support has contributed to the growth of the industry [1]. Lithium-ion batteries, the heart of EVs, are highly sensitive to temperature [2]. The capacity of the battery will improve as the temperature varies within a specified range. However, the speed of irreversible reactions will accelerate inside the battery when the temperature becomes too high, leading to a decrease in capacity and the generation of a large amount of heat in the battery simultaneously [3]. At high temperatures, lithium-ion battery performance may degrade substantially, and thermal runaway may occur, causing fires or explosions and threatening the safety of people and property [4]–[6]. At present, research in the field of EVs mainly focuses on battery management systems (BMS) and battery thermal management systems (BTMSs) [7]. The purpose of deploying a BMS for EVs is to ensure optimal performance and operational safety of the system, with state-of-charge (SOC) estimation and state-of-health (SOH) monitoring being the two most important tasks [8], [9]. Similarly, deploying BTMSs for thermal monitoring of batteries serves the same purpose as with BMS. Therefore, research on efficient and effective BTMSs is extremely urgent in the EV industry.

BTMSs have developed considerably in recent years, especially in the areas of the selection of cooling methods, optimization of channels for different cooling medium and simplification of the battery pack structure. At present, battery thermal management methods are split into 4 categories

The associate editor coordinating the review of this manuscript and approving it for publication was Xinyu Du.

according to different heat transfer media: air cooling, liquid cooling, phase change material (PCM) cooling, and heat pipe cooling. Regarding liquid cooling, the liquid medium removes heat from battery, and it has an excellent cooling performance. However, the structure of the liquid cooling device is rather complex, and liquid leakage is difficult to avoid [10]. PCM cooling has good temperature control and ensures a uniform temperature in lithium-ion batteries, and most lithium polymer batteries exhibit significant reversible thermal effects, but this method suffers from a lack of thermal conductivity [11]. Heat pipe cooling has a series of advantages, such as a high heat dissipation efficiency, fast thermal response, good isothermal performance, and flexible structure [12]. However, this method is still in the experimental stage in the field of thermal management, and its application ability is not strong. Air cooling is the earliest structure used heat dissipation systems, due to its simple structure, low cost, light weight, and easy maintenance. Air cooling is divided into two types: natural air cooling and forced air cooling [13], [14]. Natural air cooling has a slow rate of heat dissipation, which does not fulfil the requirements of BTMSs [15], whereas forced air cooling has the advantages of a low cost, superior cooling effect, and a simple structure, making it a better alternative.

Many optimization strategies have been used for the BTMS based on forced air cooling to reduce the tremendous amount of heat generated, which includes the arrangement of the batteries and fans and the design of the airflow channel. Soparat *et al.* optimized the structure of heat dissipation based on simulation results, which considered the effects of the fan arrangement and air outlet position on the temperature distribution of the battery pack [16]. Yang *et al.* analyzed the phenomenon of substantially different temperatures among the cells and designed the structure to change the air inlet angle and the wind speed, where the air intake form of blast cooling and exhaust cooling were used [17]. Wang *et al.* studied different groups of 18650 lithium-ion batteries [18]. The best temperature field distribution effect was achieved when the cylindrical lithium batteries were arranged in a circle by analyzing the temperature field. Mahamud *et al.* designed a flap valve to control the air flow that reduces the cell temperature at the outlet when the air temperature increases during the flow process [19]. Mohammadian *et al.* integrated a heat sink in the channel to improve heat dissipation and studied the effects of discharge rate, initial temperature, and flow rate on the overall temperature distribution of the battery pack [20]. Anthony Jarrett *et al.* designed a serpentine cooling channel to adapt the pressure drop of the flow field and optimized the cooling performance by changing the position of the channel [21]. Xie *et al.* employed a single factor analysis and orthogonal test method to optimize the structure of three parameters, discovering that the layout of the air flow channels exerts a significant effect on temperature, with the maximum temperature decreasing by 12.82% compared with the temperature of the initial structure [22]. Paul Nelson designed a parallel airflow channel between the cells using the auxiliary device of the heat dissipation system of air cooling to attenuate the inconsistent temperature between cells [23]. Zhang *et al.* used natural air cooling combined with a forced air-cooling strategy to reduce the extreme heat, improve the transient thermal power of batteries and prolong the lifetime of batteries using a longitudinal airflow, resulting in a depth of discharge of 84.2% [24]. In summary, unique heat dissipation structures and optimizations of essential parameters are inferred to have the ability to improve the performance of BTMS based on the studies described above. However, few systematic studies have been conducted to assess accuracy of the battery model, the mechanism of battery medium transmission, and the optimization strategy for the battery heat dissipation structure. As a result, this research focuses on the thermodynamic analysis of lithium-ion battery packs and the optimization of heat dissipation structures based on thermodynamic theory.

In this paper, a lithium-ion phosphate battery is chosen for analysis. First, a numerical model of lithium-ion batteries is established based on the heat generation and heat transfer mechanisms of lithium-ion batteries. Afterwards, Fluent is used to create a thermal model of a battery cell. The battery thermal simulation is analyzed based on the thermal characteristics of a lithium-ion battery at various discharge rates and ambient temperatures, while the validity of the model is confirmed by comparing simulation results with experimental results. Then, the simulation model of a pure EV and the model used to calculate the heat generation rate of the battery pack under typical cycling conditions are established using ADVISOR, obtaining the dynamic performance and real-time heat generation rate of the battery. Then, the heat dissipation structure is designed. Finally, the effects of the air flow rate, airflow channel spacing between cells, and air inlet angle on the temperature distribution of the battery pack are analyzed and optimized using back propagation neural network-genetic algorithms (BPNN-GA) to ensure the consistency of the temperature distribution between the battery cells, while the effectiveness of the optimized structure is highlighted through comparative experiments. The organization of the paper is described below. Section II presents the derivation and establishment of the numerical battery model. Section III presents the thermodynamic analysis of a battery cell. Section IV presents the heat generation characteristics and thermal temperature field simulation of the battery pack. The structural optimization of lithium-ion battery packs and comparative experiments are described in Section V, followed by a discussion of conclusions in Section VI.

II. ESTABLISHMENT OF THE NUMERICAL MODEL OF LITHIUM-ION BATTERIES

A. THE STRUCTURE AND WORKING PRINCIPLE OF LITHIUM-ION BATTERIES

In the course of the charging and discharging process of lithium-ion batteries, lithium ions experience intercalation and deintercalation cycles and shuttle in the

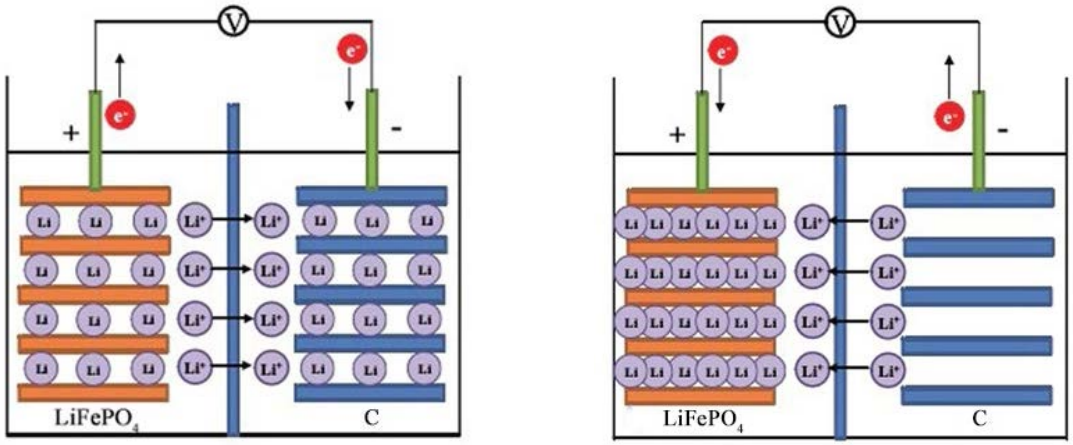

FIGURE 1. The process of charging and discharging of lithium-ion. (a) Charging process. (b) Discharging process.

electrolyte as charge carriers in the internal circuit. The oxidation–reduction reaction occurs on the electrode during lithium ion intercalation and deintercalation to generate electrons, which move directionally via the external circuit to form the electric current. Fig. 1 shows the chemical reactions of the lithium ion phosphate between the battery charging and discharging processes.

The chemical reaction of the anode is shown in (1).

$$\mathrm{LiFePO_4} \underset{discharging}{\overset{charging}{\rightleftharpoons}} x\mathrm{Li^+} + xe^- + \mathrm{Li_{(1-x)}FePO_4} \tag{1}$$

The chemical reaction of the cathode is shown in (2).

$$6\mathrm{C} + x\mathrm{Li^+} + xe^- \underset{discharging}{\overset{charging}{\rightleftharpoons}} \mathrm{Li_xC_6} \tag{2}$$

The whole chemical reaction is shown in (3).

$$\mathrm{LiFePO_4} + 6\mathrm{C} \underset{discharging}{\overset{charging}{\rightleftharpoons}} \mathrm{Li_{(1-x)}FePO_4} + \mathrm{Li_xC_6} \tag{3}$$

B. HEAT GENERATION MODEL

In the course of the charging and discharging process, complex electrochemical reactions, charge transfer, and material transfer processes occur. Their heat production is primarily composed of the reaction heat (Q_r) due to the redox process within the battery, the Joule heat (Q_J) produced by the current flowing through the internal resistance of the battery, the polarization heat (Q_P) generated by the polarization of the positive and negative electrodes due to current flowing through them, and the side reaction heat (Q_s) generated by additional reactions such as self-discharge and electrolyte decomposition. Equation (4) depicts the total heat generated (Q) in the battery pack:

$$Q = Q_r + Q_j + Q_P + Q_s \tag{4}$$

The chemical reaction of a cell at a particular temperature and pressure obeys the second law of thermodynamics, and the reaction heat is related to the operational temperature of the battery and the entropy change during the chemical reaction. When the electrochemical reaction during charging is an endothermic reaction, the reaction heat is negative; when the electrochemical reaction during discharging is an exothermic reaction, the reaction heat is positive. The reaction heat is calculated using (5):

$$Q_r = ItT\left(\frac{\partial E}{\partial T}\right)_P \tag{5}$$

where I represents the battery working current; t represents the battery working time; T represents the thermodynamic temperature; E represents the battery electromotive force, i.e., the open circuit voltage of the battery; and P represents pressure.

The Joule heat is related to the ohmic resistance of the internal materials of the battery and is a positive value during the charging and discharging process, which meets Joule's law and is represented in (6):

$$Q_j = I^2 R_j t \tag{6}$$

where R_j represents the ohmic resistance of the battery.

When current flows inside the battery, the electrode potential deviates from the equilibrium potential, which is defined as polarization. Polarization will produce difference in potential with heat generation. The amount of heat generated is proportional to the internal resistance of the battery to polarization. The value of polarization heat is positive during the charging and discharging process, as shown in (7):

$$Q_P = I^2 R_P t \tag{7}$$

where R_P represents the polarized internal resistance of the battery.

The proportion of side reaction heat generated during the charging and discharging of lithium-ion batteries is so small

TABLE 1. Technical parameters of SE100AHA square lithium-ion phosphate battery.

Parameters	Value	Parameters	Value
Length×width×height	144×66×218mm	Internal resistance	≤1mΩ
Weight	3.3±0.1kg	Self-discharge rate	≤3%
Rated capacity	100Ah	Charge cut-off voltage	3.65V
Rated voltage	3.2V	Discharge cut-off voltage	2.5V

TABLE 2. Thermo-physical parameters of the LiFePO4 battery.

Item	Density ρ $\left(\mathrm{kg/m^3}\right)$	Specific heat C_p $\left(\mathrm{J/(kg\cdot K)}\right)$	Thermal conductivity λ $\left(\mathrm{W/(m\cdot K)}\right)$
Positive pole (Al)	2702.5	871.5	236.0
Negative pole (Cu)	8935.0	381.0	398.0
Core	3000	1100	x: 0.91; y、z: 2.73

that it can be ignored. As a result, the total heat generation can is calculated using (8):

$$Q = ITT\left(\frac{\partial E}{\partial T}\right)_P + I^2R_jt + I^2R_pt \tag{8}$$

The corresponding heat production per unit time and unit volume is calculated using Equations (4)-(8) and the model proposed by Bernardi [25]as shown in (9):

$$q = \frac{I}{V}\left[T\frac{\partial E}{\partial T} + I\left(R_j + R_p\right)\right] \tag{9}$$

where V represents the battery volume.

C. HEAT TRANSFER MODEL

The heat transfer model of lithium-ion batteries consists of 3 parts: thermal conduction, thermal convection, and thermal radiation [26]. Chemical reactions inside the battery generate heat during charging and discharging processes. Part of the heat is transferred to the surface of the battery by thermal conduction through the internal materials of the battery, and then the heat is transferred to the cooling fluid and the surrounding environment by thermal convection and thermal radiation, respectively. The other part of the heat is absorbed by the internal materials of the battery, causing the temperature to increase.

The non-steady-state thermal conduction differential equation is established based on the law of energy conservation and Fourier, as illustrated in (10):

$$\rho c\frac{\partial T}{\partial t} = \frac{\partial}{\partial x}\left(\lambda\frac{\partial T}{\partial x}\right) + \frac{\partial}{\partial y}\left(\lambda\frac{\partial T}{\partial y}\right) + \frac{\partial}{\partial z}\left(\lambda\frac{\partial T}{\partial z}\right) + q \tag{10}$$

where ρ represents the density of battery cells; c represents the specific heat capacity of the battery cell; x, y, and z represent the x, y, and z directions in the Cartesian coordinate system, respectively; λ represents the thermal conductivity of battery cells; and q represents the value of heat produced by the battery per unit time and unit volume.

Thermal convection only occurs in fluids (gas and liquids), which must be accompanied by heat conduction caused by the movement of fluid molecules. The convective heat of the battery is always a positive value since the surface temperature of the battery is always higher than that of the cooling fluid during normal battery operation. The formula used to calculate the convective heat on the battery surface adopts Newton's law of cooling, as shown in (11):

$$q_e = h\left(t_w - t_f\right) \tag{11}$$

where q_e represents the heat flow density; h represents the surface heat transfer coefficient; and t_w and t_f are the temperature of the battery surface and that of the cooling fluid, respectively.

Radiation heat exchange accounts for a relatively small part of the overall heat of the battery due to the modest temperature difference between the battery and the surrounding environment. As a result, radiation transfer heat is normally ignored in calculations.

III. THERMODYNAMIC ANALYSIS OF THE LITHIUM-ION BATTERY CELL

The SE100AHA square lithium-ion phosphate battery, which is manufactured by a Chinese company and chosen for this study. The technical parameters of the battery used are shown in Table 1, while the thermodynamic parameters are described in Table 2 [27], [28].

The structure of the battery is simplified to a reasonable degree to reduce the simulation complexity and ensure meshing quality. The core, positive pole (P), and negative pole (N) are built into a model of the cell. Meanwhile, the intersection of the two diagonal lines on the front of the battery is regarded as the center point of the surface, namely, measuring point (O), as shown in Fig.2.

A. ESTABLISHMENT OF GOVERNING EQUATIONS

ANSYS Fluent is used for the simulation and analysis of the lithium-ion battery cell based on the computational fluid dynamics (CFD) method. In this research, the battery is cooled by air, and thus the heat transfer and fluid flow processes in the battery pack are components of the open system,

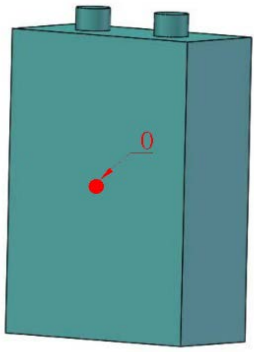

FIGURE 2. The model of the battery cell.

which follows the continuity equation, momentum equation, and energy equation, as shown in (12)-(14), respectively:

$$\frac{\partial \rho}{\partial t} + \frac{\partial (\rho u)}{\partial x} + \frac{\partial (\rho v)}{\partial y} + \frac{\partial (\rho w)}{\partial z} = 0 \tag{12}$$

where ρ represents the density; u, v, and w denote the components of the velocity vector in the x, y and z directions, respectively.

$$\begin{cases} \frac{\partial (\rho u)}{\partial t} + div(\rho U u) = div(\eta grad u) - \frac{\partial p}{\partial x} + S_u \\ \frac{\partial (\rho v)}{\partial t} + div(\rho U v) = div(\eta grad v) - \frac{\partial p}{\partial y} + S_v \\ \frac{\partial (\rho w)}{\partial t} + div(\rho U w) = div(\eta grad w) - \frac{\partial p}{\partial z} + S_w \end{cases} \tag{13}$$

where U represents the velocity vector; η represents the dynamic viscosity of the fluid; p represents the pressure on the fluid element; and S_u, S_v and S_w denote the generalized source terms of the momentum equation.

$$\frac{\partial (\rho T)}{\partial t} + div(\rho U T) = div\left(\left(\frac{k_{eff}}{c_p}\right) grad T\right) + S_h \tag{14}$$

where c_p represents the specific heat capacity under constant pressure; k_{eff} represents the effective heat transfer coefficient of the fluid; and S_h denotes the heat of the chemical reaction and other user-defined volumetric heat source items.

When the Reynolds number is larger than the critical Reynolds number (2000–3000), the state in the battery box is turbulent. For turbulent motion, the standard model $k-\varepsilon$ is commonly used as follows:

$$\begin{aligned} \frac{\partial (\rho k)}{\partial t} + \frac{\partial (\rho k u_i)}{\partial x_i} &= \frac{\partial}{\partial x_j}\left[\left(\mu + \frac{\mu_t}{\sigma_k}\right)\frac{\partial k}{\partial x_j}\right] \\ &\quad + \mu_t\left(\frac{\partial u_i}{\partial x_j} + \frac{\partial u_j}{\partial x_i}\right)\frac{\partial u_i}{\partial x_j} \\ &\quad - \rho\varepsilon + S_k \end{aligned} \tag{15}$$

$$\begin{aligned} \frac{\partial (\rho \varepsilon)}{\partial t} + \frac{\partial (\rho \varepsilon u_i)}{\partial x_i} &= \frac{\partial}{\partial x_j}\left[\left(\mu + \frac{\mu_t}{\sigma_\varepsilon}\right)\frac{\partial \varepsilon}{\partial x_j}\right] \\ &\quad + C_{1\varepsilon}\mu_t\left(\frac{\partial u_i}{\partial x_j} + \frac{\partial u_j}{\partial x_i}\right)\frac{\partial u_i}{\partial x_j} \\ &\quad - C_{2\varepsilon}\rho\frac{\varepsilon^2}{k} + S_\varepsilon \end{aligned} \tag{16}$$

where k represents the turbulent kinetic energy; ε represents the turbulent energy dissipation rate; σ_k and σ_ε are the Prandtl numbers for k and ε, respectively; S_k and S_ε are user-defined source terms; $C_{1\varepsilon}$ and $C_{2\varepsilon}$ are empirical constants; and μ_t represents the turbulent viscosity, which can be calculated as follows:

$$\mu_t = \rho C_\mu \frac{k^2}{\varepsilon} \tag{17}$$

where C_μ is a constant, and the values of empirical constants are calculated using the following equation: $C_{1\varepsilon} = 1.44$, $C_{2\varepsilon} = 1.92$, $C_\mu = 0.09$, $\sigma_k = 1.0$, $\sigma_\varepsilon = 1.0$.

B. TEMPERATURE DISTRIBUTION OF THE BATTERY CELL

In Fluent, when the discharging test is performed, the initial temperature is 25 °C, and the discharge rates are 1.0 C and 1.5 C, respectively. The simulation results are shown in Fig.3. The temperature of the battery center is visibly the greatest, and it progressively decreases towards the edge. Upon discharging to the cut-off voltage at a rate of 1.0 C, the peak temperature is 41.95 °C, and the lowest temperature is 38.44 °C, which increases by 16.95 °C and 13.44 °C, respectively, compared to the initial battery temperature. Meanwhile, the maximum temperature difference is 3.51 °C. When the discharge rate is 1.5 C, the highest and lowest temperatures on the battery surface are 48.66 °C and 43.76 °C respectively, which increase by 23.66 °C and 18.76 °C, respectively. In addition, the maximum temperature difference on the surface reaches 4.90 °C. Overall, as the discharge rate increases, the value of heat generation and the temperature difference of the battery increase.

The simulation result of setting the discharge rate to 1.0 C and the initial temperature to 45 °C is shown in Fig.4. In this situation, the battery has a maximum temperature of 58.43 °C and a minimum temperature of 55.03 °C, while the temperature of the battery surface is greater than the upper limit of the normal operating temperature. Furthermore, as the initial temperature increases, the temperature of the battery increases substantially, since the rate of chemical reaction accelerates in a higher-temperature environment, generating a considerable amount of reaction heat. As heat accumulates in the battery, the temperature increases, potentially reducing the lifespan and capacity of the battery while also causing a safety risk. Hence, conducting and improving battery thermal management are particularly important.

C. MODEL VERIFICATION

In accordance with the temperature field distribution of the battery, a trend towards an increasing temperature trend from the edge to the center of the core is observed. The temperature of measurement point O is positioned in the center of the battery surface, where the highest surface temperature is measured. As a result, the temperature at measurement point O is chosen as a critical point to test the reliability and validity of the model. The simulated temperature data

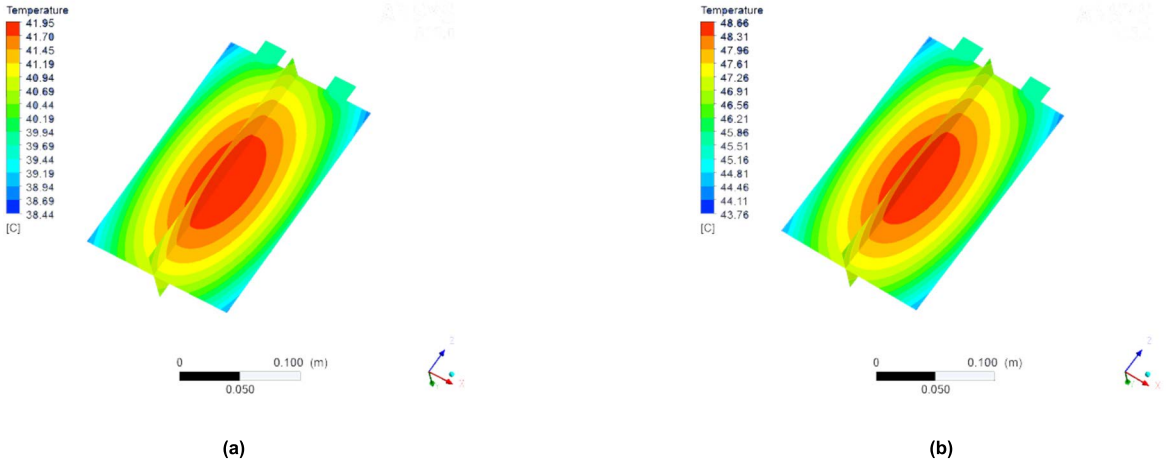

(a) (b)

FIGURE 3. Temperature distribution at different discharge rates (initial temperature of 25 °C). (a) Simulation results at 1C. (b) Simulation results at 1.5 C.

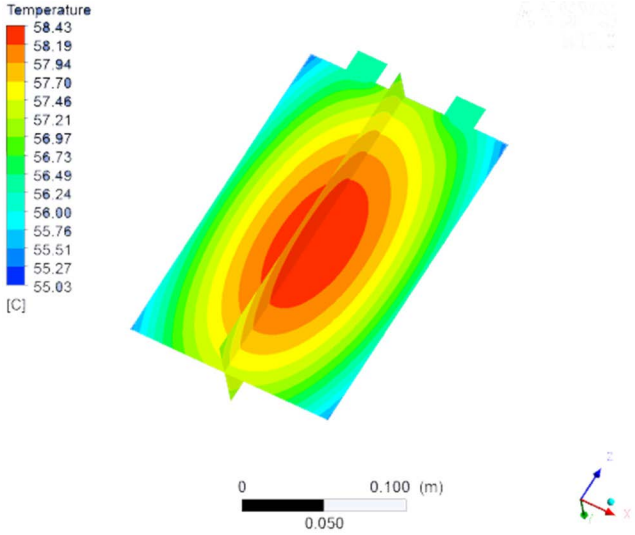

FIGURE 4. Temperature distribution at 45 °C (discharge rate of 1 C).

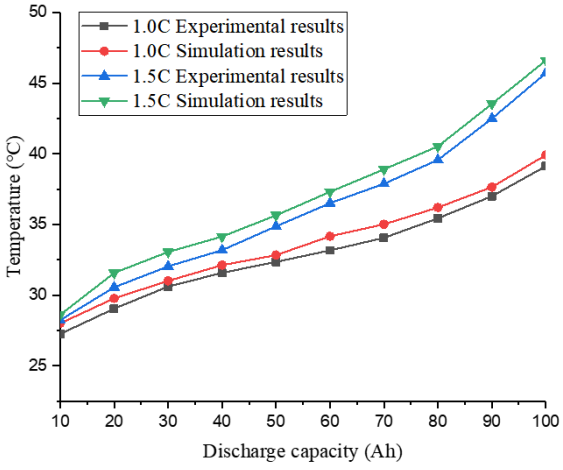

FIGURE 5. Comparison between simulation results and experimental results at different discharge rates.

from point O are compared with the experimental data at different discharge rates, with the initial temperature set to 25 °C, as shown in Fig. 5. The trends of the simulation and experimental results are basically consistent under different discharge rates, and the simulation data are slightly higher than the experimental data. Measurement point O reaches the maximum temperature of 39.14 °C at the discharge rate of 1 C and during the end period of the discharge process in the experimental data, which is only 0.78 °C lower than the simulation data. When the discharge rate is adjusted to 1.5 C, the maximum difference between the simulation data and the experimental data is 0.89 °C. The error may be caused by the heat transfer coefficient, which is obtained from empirical values when setting the boundary conditions. If the coefficient is selected to be slightly lower, the simulation result will be slightly higher than the experimental result. In general, the error is small, which meets the error range requirement of 5% [29]. At the same time, the simulation results are higher than the experimental results, implying that the battery will operate in a wider temperature range, which exerts a significant positive effect on the design of the BTMS.

The experimental and simulation temperature data from the measurement point O at 25 °C and 45 °C are chosen for comparison, as shown in Fig. 6. The experimental data and simulation data obtained at different temperatures are basically consistent, with the maximum temperature difference between the experimental data and the simulation data of 0.62 °C at the initial temperature of 25 °C and 0.87 °C at the initial temperature of 45 °C. Therefore, the error is small, which validates the effectiveness of the model and further illustrates that the use of Fluent to simulate the battery temperature field is feasible.

TABLE 3. Technical parameters of pure EV.

Parameters	Value	Parameters	Value
Vehicle size	3655×1650×1550 mm	Weight（kg）	1268 kg
Frontal area	2.3 m^2	Drag coefficient	0.3
Spread of axles	2370 mm	Track front / rear	1400/1385 mm
Rolling radius	282 mm	Transmission efficiency	90%

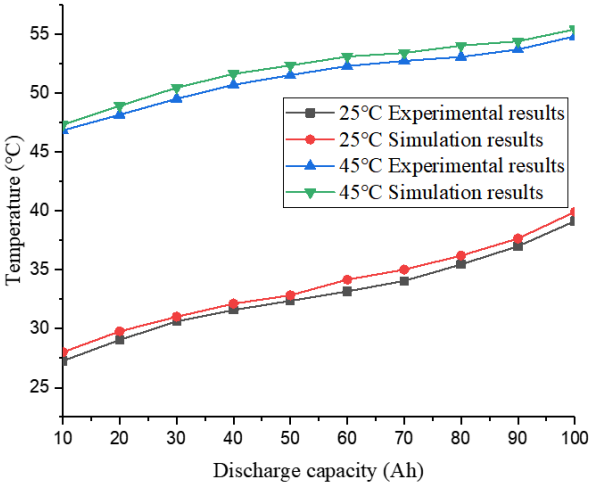

FIGURE 6. Comparison between simulation results and experimental results at different temperatures.

IV. HEAT GENERATION CHARACTERISTICS AND TEMPERATURE FIELD SIMULATION OF THE BATTERY PACK

A. DYNAMIC CHARACTERISTICS OF THE BATTERY PACK

Normally, the static performance test is used to obtain the thermal characteristics of battery packs [30]. However, the heat generation is closely related to the battery internal characteristics and the external environment. Additionally, changes in parameters such as SOC and ambient temperature may affect battery pack performance. Therefore, the static performance test is unable to accurately estimate heat generation, and a dynamic performance simulation should be performed. ADVISOR software is used to simulate the dynamic performance of pure EVs to obtain the real-time heat generation rate of the battery pack under typical working condition. The technical parameters of the pure EV model used for the simulation are shown in Table 3.

The model of the pure EV battery pack is built in SIMULINK, as shown in Fig. 7. The modules of the heat generation rate and the calculation of heat generation in the battery pack are built, as shown in the area marked by the dotted frame in Fig.7. Usually, the submodules of the heat generation rate and the calculation of heat generation are not considered while the heat generation and heat dissipation of each cell in the battery pack are uniform in the temperature calculation module, which ignores the effects of the battery characteristics and the structural parameters of the heat dissipation. Therefore, the module must be modified based on the current, temperature and internal resistance. The actual heat generation of the battery is calculated using Equation (9), considering the characteristics of internal resistance.

The condition of CYC_ECE_EUDC (Cycle-Economic Commission for Europe-Extra Urban Driving Cycle) is selected because EVs work in complex road conditions. And compared with other working conditions, the selected working condition is more complicated, which meets the requirements of our simulation purpose. CYC_ECE_EUDC consists of 4 Economic Commission for Europe (ECE) conditions and an extra urban driving cycle (EUDC) condition. The total mileage in this working condition is 10.93 km, which lasts 1225 s, the maximum speed is 120 km/s, the average speed is 32.1 km/s, the maximum acceleration is 1.06 m/s^2, and the maximum deceleration is -1.39 m/s^2. At the same time, 13 stops occur during the driving, and the idling time is 339 s. The simulation results are shown in Fig. 8. When the speed is maintained at less than approximately 50 km/h, the output of the current is basically stable; however, the current fluctuates considerably at speeds ranging from 60–120 km/h. When the EV reaches the maximum driving speed, the current reaches the maximum value of 140 A. The battery pack current increases as the EV accelerates while running at a high speed. The heat generation rate of the battery pack is low under urban road conditions. Nevertheless, the heat generation rate increases substantially under the sub-urban road condition as the output power increases, which may reach a maximum value of 24000W/m^3. Therefore, the performance requirements of the battery pack heat dissipation system are more stringent under the condition of the extra urban condition and high driving speed.

The content mentioned above is collectively referred to as the thermal analysis model of the battery. In quite a lot of studies, only the numerical model of the battery is established to conduct the simulation study of the battery pack, and the thermodynamic analysis of the lithium-ion battery cell and the verification of the established model are rarely carried out. Meanwhile, only a few researches consider the heat generation characteristics of the battery. Therefore, the comparative analysis of different techniques is presented in Table 4 (in the table, represents the model contains the attribute and × represents the model does not contain) to highlight the advantages of the battery thermal analysis model used in the paper compared to the mainstream models. The attributes in Table 4 are considered important for thermal analysis of

TABLE 4. Comparison of important attributes for the battery thermal analysis models.

Thermal analysis model	Numerical model of lithium-ion batteries	Thermodynamic analysis of a battery cell	Verification of the established model	Consideration of heat generation characteristics
Soparat *et al.* [16]	✓	×	×	✓
Wang *et al.* [18]	✓	×	✓	×
Xu *et al.* [31]	✓	✓	✓	×
Sun *et al.* [32]	✓	×	×	×
Proposed model	✓	✓	✓	✓

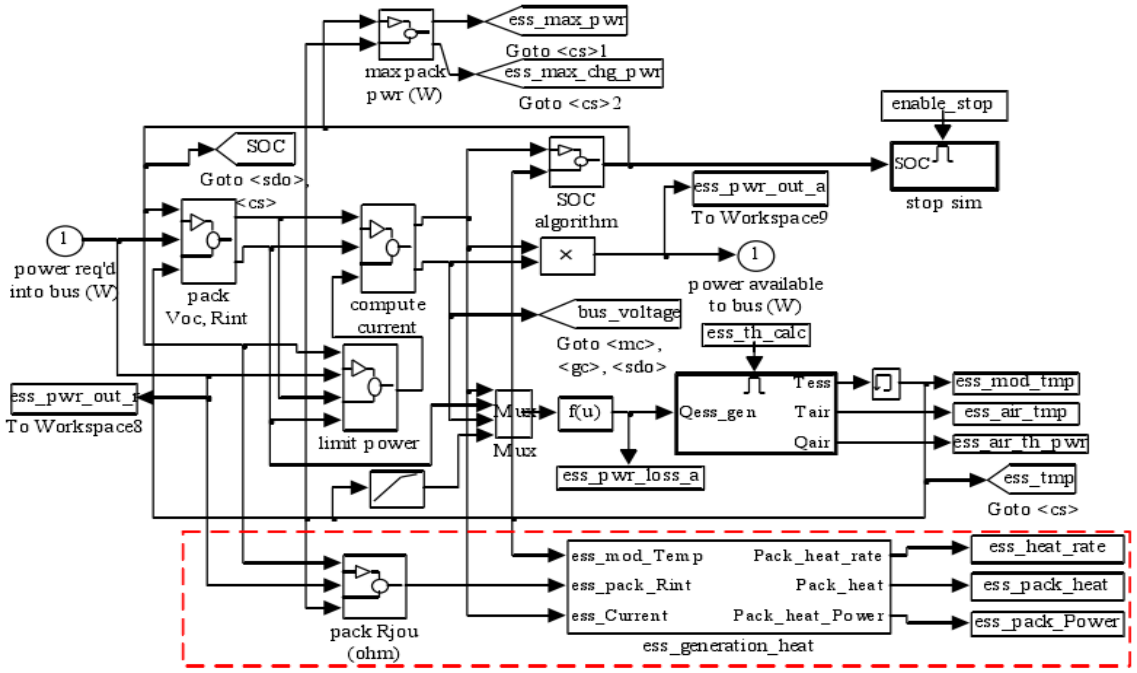

FIGURE 7. The simulation model of a pure EV.

a lithium-ion battery. An effective strategy for the thermal analysis of a lithium-ion battery should have the following attributes: (i) establishes an accurate numerical model of lithium-ion batteries including heat generation model and heat transfer model, (ii) conducts the thermodynamic analysis of the lithium-ion battery cell based on the establishment of governing equations and the analysis of temperature distribution of a battery cell, (iii) verifies the battery model at different discharge rates and different temperatures, and (iv) takes into account the heat generation characteristics in the dynamic characteristics of the battery pack. Based on the experimental work presented in this paper, the proposed battery thermal analysis model features the above-mentioned attributes and, thus, is suitable for the thermodynamic analysis of lithium-ion batteries.

B. HEAT DISSIPATION TEMPERATURE FIELD SIMULATION OF THE BATTERY PACK

The heat dissipation structure of a Li-ion battery pack should be designed with the goal of not only adapting heat dissipation during peak power but also ensuring temperature consistency between battery cells. Therefore, the heat dissipation structure is designed through comprehensive considerations and comparisons. In the structure, 8 prismatic battery cells are connected in series to form a battery pack with parallel ventilation, the inlet angle is 8° and the gas channel spaces are 4 mm with equal intervals. The overall heat dissipation structure is shown in Fig. 9

In ANSYS, the automatic meshing module is used for meshing the model of the battery pack. The fluid domain of the simulation model is established using Fluent. The wind speed and the initial temperature are set to 4 m/s and 25 °C, respectively. The simulation results are displayed in Fig. 10, which shows that the lowest temperature of the battery pack is 34.65 °C and the highest temperature is 45.04 °C, with a maximum temperature difference of 10.39 °C within the battery pack. The explanation for this phenomenon is that the cooling air may transport a large amount of heat after heat exchange with multiple battery cells in order, even if the cooling air temperature is low at the air inlet. As a result, the heat exchange capacity is greatly reduced, causing a temperature difference in the cells. Meanwhile, most of the

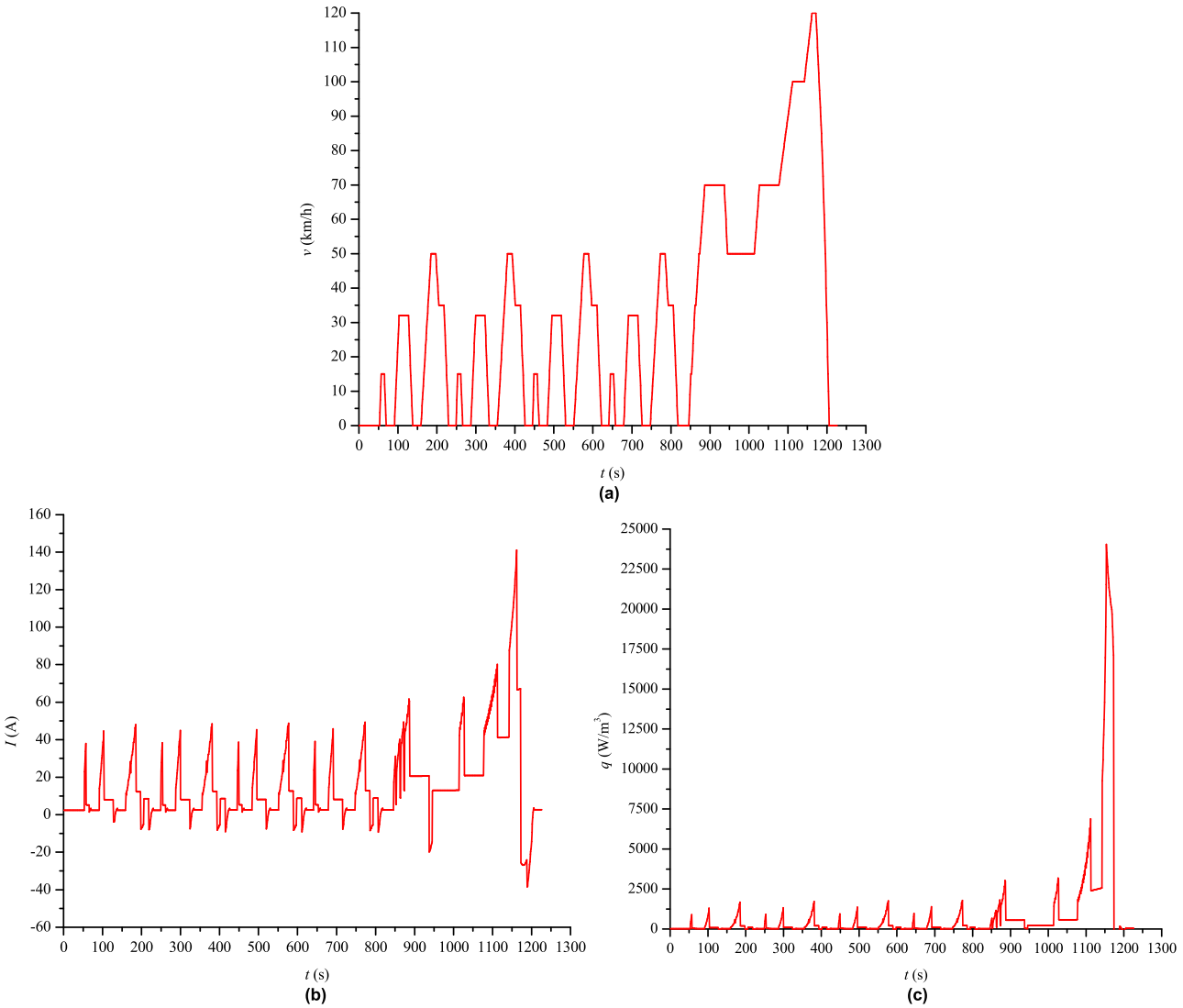

FIGURE 8. The simulation results under CYC_ECE_EUDC working condition by using ADVISOR. (a) The curve of speed. (b) The curve of current. (c) The curve of heat generation rate.

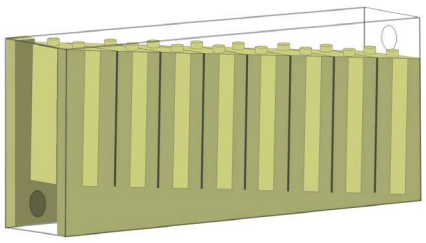

FIGURE 9. The structure of the battery pack.

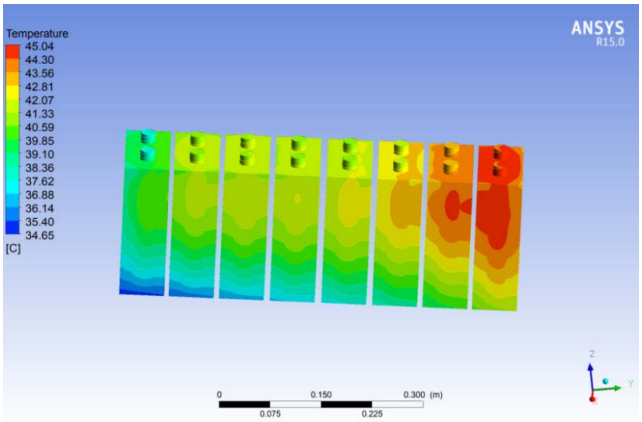

FIGURE 10. Simulation results of the battery pack.

battery pack has a temperature greater than 40 °C. Although the temperature is still within the safe temperature range of the lithium-ion battery, it exceeds the upper limit of the ideal temperature range. In these situations, the temperature may reduce the performance of the battery when operating at these temperatures for a long time, which may increase the inconsistency of the temperature between cells and shorten lifespan of the battery pack. As a result, further optimization of the heat dissipation structure is needed.

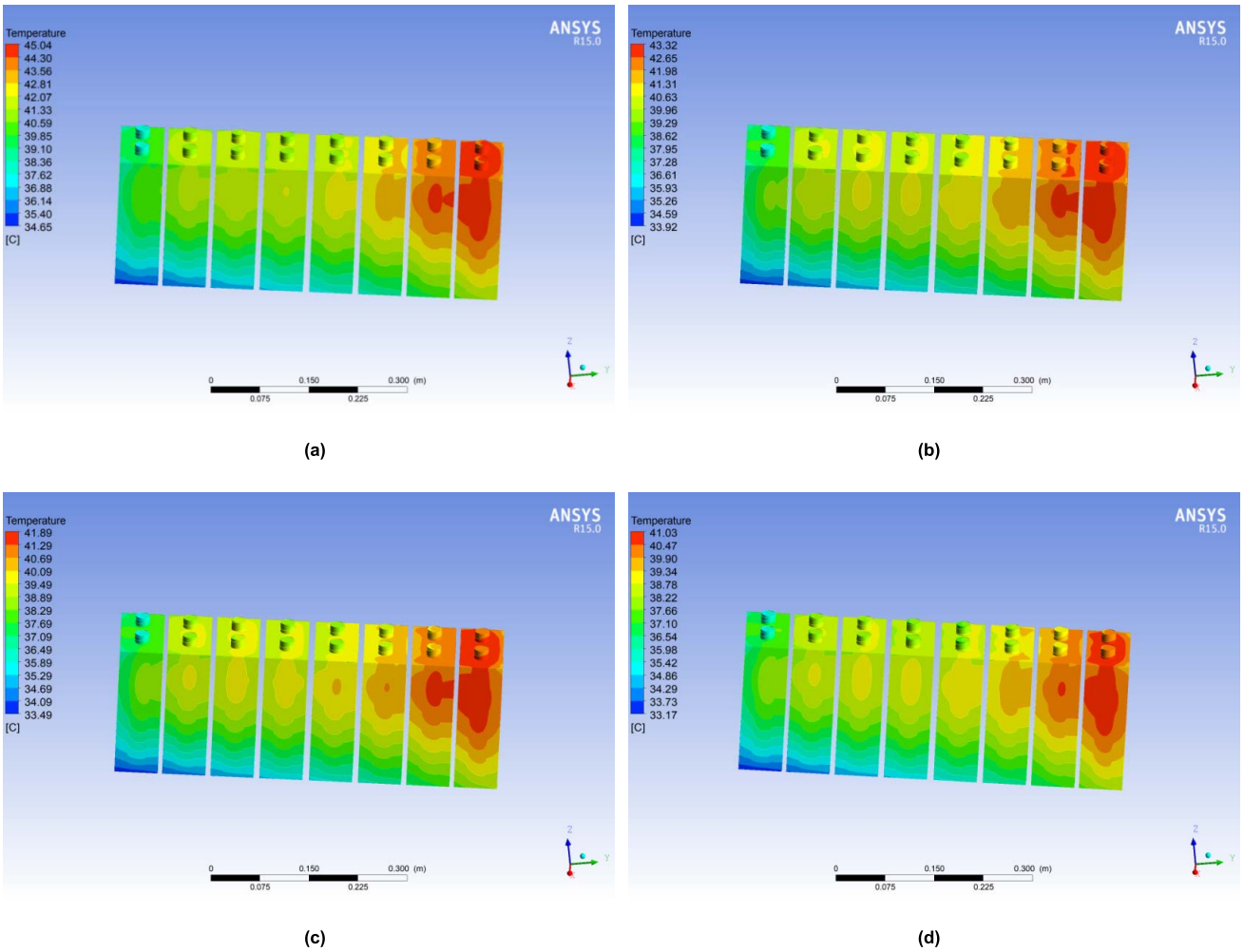

FIGURE 11. Simulation results under different rate of cooling air flow. (a) Setting the cooling air flow at 4m/s. (b) Setting the cooling air flow at 5m/s. (c) Setting the cooling air flow at 6m/s. (d) Setting the cooling air flow at 7m/s.

V. STRUCTURAL OPTIMIZATION FOR THE LITHIUM-ION BATTERY PACK

A. EFFECTS OF THE WORKING PARAMETERS ON HEAT DISSIPATION

The initial temperature is set to 25 °C, and the other parameters remain unchanged except for the rate of the cooling air, which is set to 4 m/s, 5 m/s, 6 m/s, and 7 m/s for the simulation calculation, as shown in Fig. 11. The battery pack temperature increases from left to right, while the overall temperature of the battery pack decreases as the rate of cooling air increases, reducing the temperature difference between the cells. When the wind speed increases from 4 m/s to 5 m/s, the maximum temperature of the battery pack decreases from 45.04 °C to 43.32 °C, and the maximum temperature difference between the cells decreases from 10.39 °C to 9.40 °C, representing a decrease of 1.72 °C and 0.99 °C, respectively. When the wind speed increases from 5 m/s to 6 m/s, the maximum temperature of the battery pack decreases by 1.43 °C, and the maximum temperature difference decreases by 0.98 °C. When the wind speed increases from 6 m /s to 7 m/s, the maximum temperature of the battery pack decreases by 0.86 °C, while the maximum temperature difference decreases by only 0.54 °C. In summary, the temperature gradually decreases as the wind speed increases.

B. EFFECTS OF THE STRUCTURAL PARAMETERS ON HEAT DISSIPATION

In the heat dissipation structure, the initial battery arrangement interval is set to 4 mm, and the tolerance is 0 mm. The structure is optimized by adopting different tolerance values. The tolerance values are set to 0.5 mm and 1.0 mm; therefore, the spacing among the flow channels increases in the battery pack. For example, when the tolerance value is 0.5 mm, the distance between each cell is 4 mm, 4.5 mm, 5 mm, 5.5 mm, 6 mm, 6.5 mm, and 7 mm. The simulation results are shown in Fig. 12. In this case, the maximum temperature is 44.62 °C, which is 0.42 °C lower than in the configuration with equal intervals, while the maximum temperature difference of the battery pack does not change noticeably. When the tolerance value is 1.0 mm, the maximum temperature of the battery

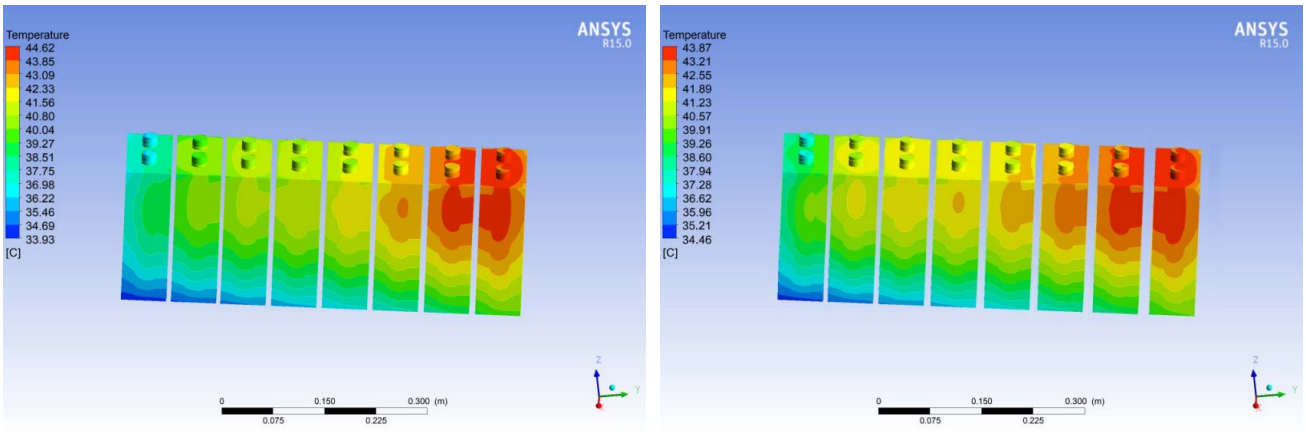

FIGURE 12. Simulation results under different spacing. (a) Setting the tolerance value at 0.5mm. (b) Setting the tolerance value at 1mm.

pack is 43.87 °C, which is 1.17 °C lower, and the maximum temperature difference is 0.98 °C lower than in the configuration with equal intervals. Hence, the heat dissipation effect and the temperature inconsistency between the batteries are gradually improved by optimizing the distance at which of the cells are arranged.

The difference in pressure explains the air flow; therefore, the effect of the pressure difference on heat dissipation is explored by changing the inlet angle. When the inlet angle is set from 8° to 5° (see Fig. 13), the maximum temperature of the battery pack increases from 45.04 °C to 46.33 °C, while the maximum temperature difference increases by 1.29 °C. Thus, if the inlet angle is appropriately set within a reasonable range, the cooling effect maybe better.

C. OPTIMIZATION OF THE HEAT DISSIPATION STRUCTURE BASED ON BPNN-GA

The heat dissipation performance of the battery pack is related to the inlet angle, the battery layout, and the cooling wind speed, based on the simulation analysis. The back propagation neural network-genetic algorithm (BPNN-GA) method is used to optimize the heat dissipation parameters, and the optimized battery pack is substituted into Fluent for analysis to obtain reasonable parameters that lower the maximum temperature of the battery pack. BPNN combined with GA to perform function extremum optimization is mainly divided into two parts: BPNN training and fitting, and genetic algorithm extremum optimization. First, a suitable BPNN is established, and the air flow rate, spacing tolerance value between battery cells, and inlet angle are used as the inputs. Meanwhile, the temperature is used as the output to train the BPNN. Then, the trained BPNN with a high goodness of fit is used to predict the temperature. BPNN is regarded as a nonlinear function [33], where the network input value and output value are the independent and dependent variables of the function, respectively. When the number of input layer nodes is m and the number of output layer nodes is n, BPNN expresses the functional mapping relationship from m independent variables to n dependent variables [34]. Any mapping relations of the m-dimension to n-dimension can be approximated by a 3-layer BPNN, but the network will become more complex and the training efficiency will decrease as the number of layers increases, although this approach can improve network accuracy [35]. Hence, the hidden layer number is set to 1. The prediction result obtained after BPNN training is used as the individual fitness value of the GA, and the global optimal value of temperature and corresponding parameter conditions are obtained through selection, crossover and mutation operations [36], [37]. Neural network training is used to optimize the objective function to ensure the lowest temperature of the system. The flow chart of the BPNN-GA method is shown in Fig.14. The orthogonal experiment is used to select representative data and reduce the number of simulations; at the same time, 3 levels and 3 factors $L_9(3^3)$ (air flow rate, spacing between battery cells and inlet angle) are applied to obtain training data. The factors and levels are shown in Table 5, where T_{MAX} denotes the maximum temperature of the battery pack. The scheme and results of the orthogonal experiment are shown in Table 6.

In this structural optimization, the trained neural network is used as the fitness function, the maximum genetic algebra is set to 100 generations, and the optimization parameter value ranges from 0 to7. Then, the minimum system temperature is obtained when setting the air flow rate to 6.58 m/s, spacing tolerance value between battery cells at 1.0 mm, and the inlet angle to 6.5°. The optimized model of the battery pack is shown in Fig. 15. The inlet angle of the optimized structure is 1.5° smaller than that of the initial structure, and the spacing between the cells is now larger than before as well.

The temperature distributions before and after structural optimization are shown in Fig. 16. The trend for

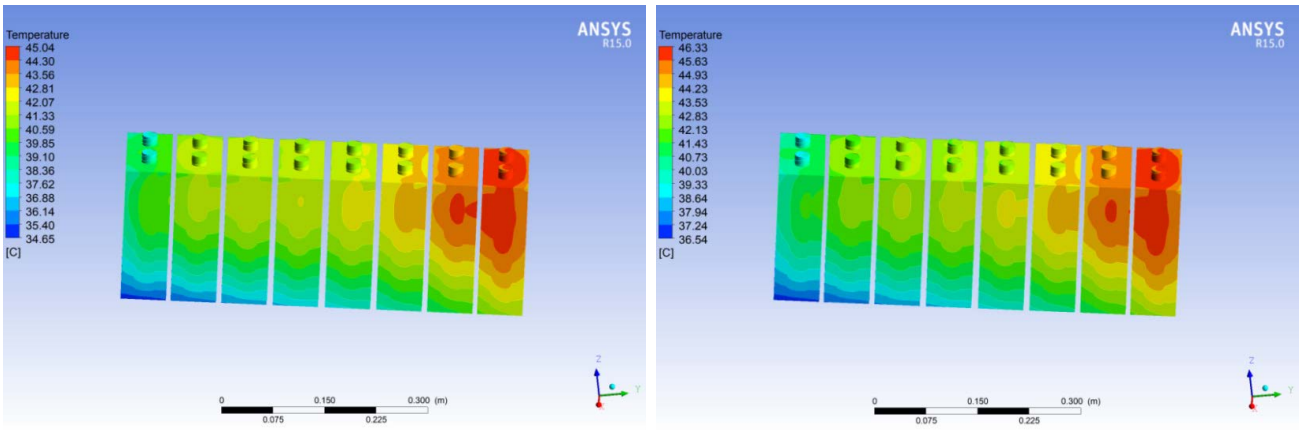

(a) (b)

FIGURE 13. Simulation results under different inlet angles. (a) Temperature distribution at 8°. (b) Temperature distribution at 5°.

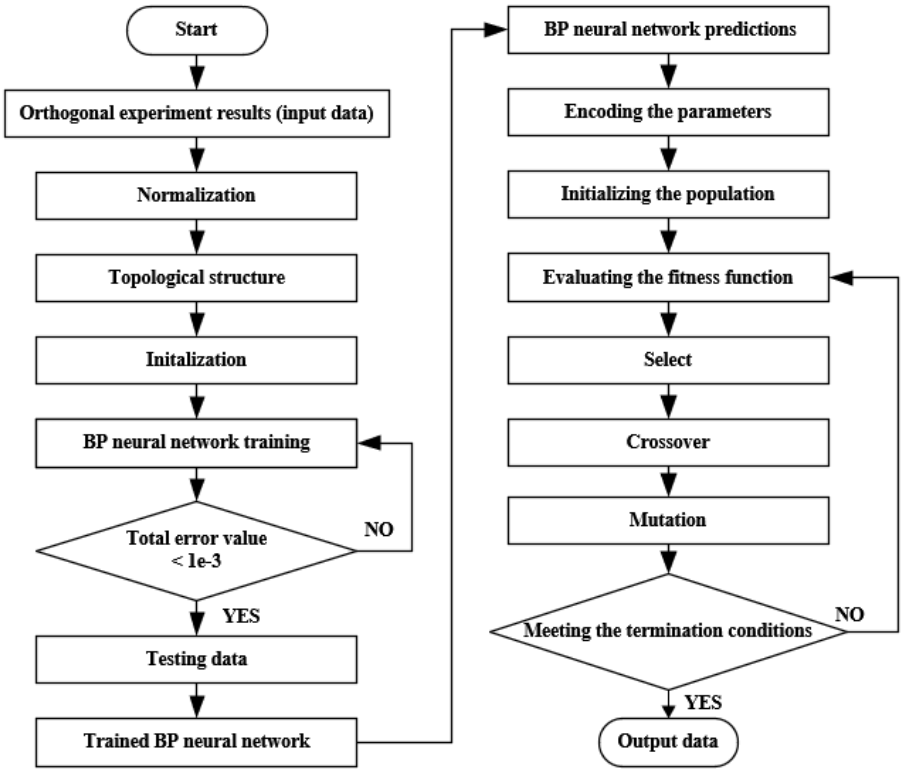

FIGURE 14. The flow chart of BPNN-GA.

the temperature distribution of the battery pack before and after optimization is basically the same. The maximum temperature of the initial structure is 45.04 °C, while that after optimization is 40.86 °C, representing a decrease of 4.18 °C. At the same time, the maximum temperature difference of the initial structure is 10.39 °C, while that of the optimized structure is 7.68 °C. The temperature of the battery pack clearly decreases after optimization, ensuring that the battery pack can operate in an appropriate temperature range and improving temperature inconsistency.

Additionally, the initial ambient temperature is set to 30 °C and 35 °C to verify the feasibility and generality of the optimized structure. The temperature distribution trend of the battery pack before and after optimization under the newly set ambient temperature is consistent with that of the ambient temperature at 25 °C. The temperature distribution

TABLE 5. Factors and levels in the orthogonal experiment.

Factor / Level	A: air flow rate	B: spacing tolerance value	C: inlet angle
1	4 m/s	0 mm	5°
2	5 m/s	0.5 mm	6°
3	6 m/s	1.0 mm	7°

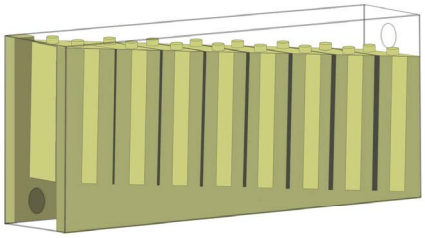

FIGURE 15. The structure of the battery pack after optimization.

of the battery pack before and after structural optimization are shown in Fig. 17. When the initial ambient temperature is set to 30 °C, the maximum temperature of the initial structure is 47.14 °C, while that after optimization is 41.29 °C, representing a decrease of 5.85 °C. At the same time, the maximum temperature difference of the initial structure is 9.91 °C, while that of the optimized structure is 7.33 °C. Similarly, when the initial temperature is set to 35 °C, the maximum temperature of the initial structure is 50.87 °C, while that after optimization is 42.93 °C, representing a decrease of 7.94 °C. At the same time, the maximum temperature difference of the initial structure is 10.48 °C, while that of the optimized structure is 6.86 °C. Therefore, it can be determined that the heat dissipation structure optimized at an ambient temperature of 25 °C can still maintain a good heat dissipation performance when the ambient temperature changes.

TABLE 6. The scheme and results of the orthogonal experiment.

Number	Factor			T_{MAX}
	A	B	C	
1	1	1	1	46.33°C
2	1	2	2	45.28°C
3	1	3	3	44.97°C
4	2	1	2	43.76°C
5	2	2	3	43.06°C
6	2	3	1	42.08°C
7	3	1	3	42.15°C
8	3	2	1	41.39°C
9	3	3	2	41.27°C

D. DISSCUSSION ON OPTIMIZATION METHODS

According to the existing battery heat dissipation structure optimization research, the optimization methods of heat dissipation structure are divided into the following categories: traditional optimization methods, multi-objective optimization methods based on orthogonal experiment, and optimization methods based on the combination of correlation algorithms [10]–[22]. Traditional optimization methods combine multiple different cooling methods to optimize the heat dissipation structure, e.g. the combination of phase change material (PCM) and pyrolytic graphite sheet and fin [32]. The heat dissipation structure obtained by this optimization method has a relatively simple structure, but its performance cannot be greatly improved, and the

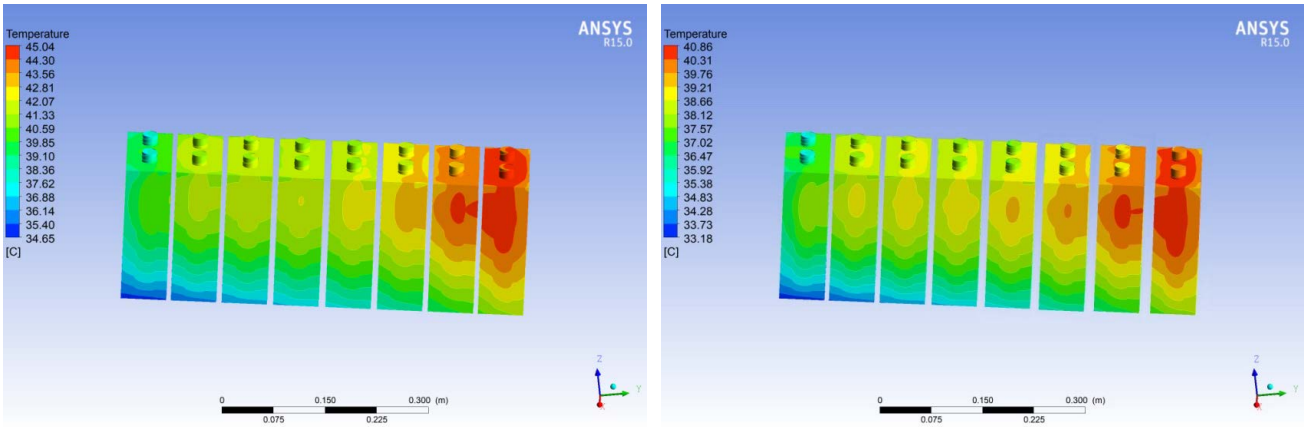

(a) (b)

FIGURE 16. Temperature distribution before and after structural optimization. (a) Initial structure. (b) Optimized structure.

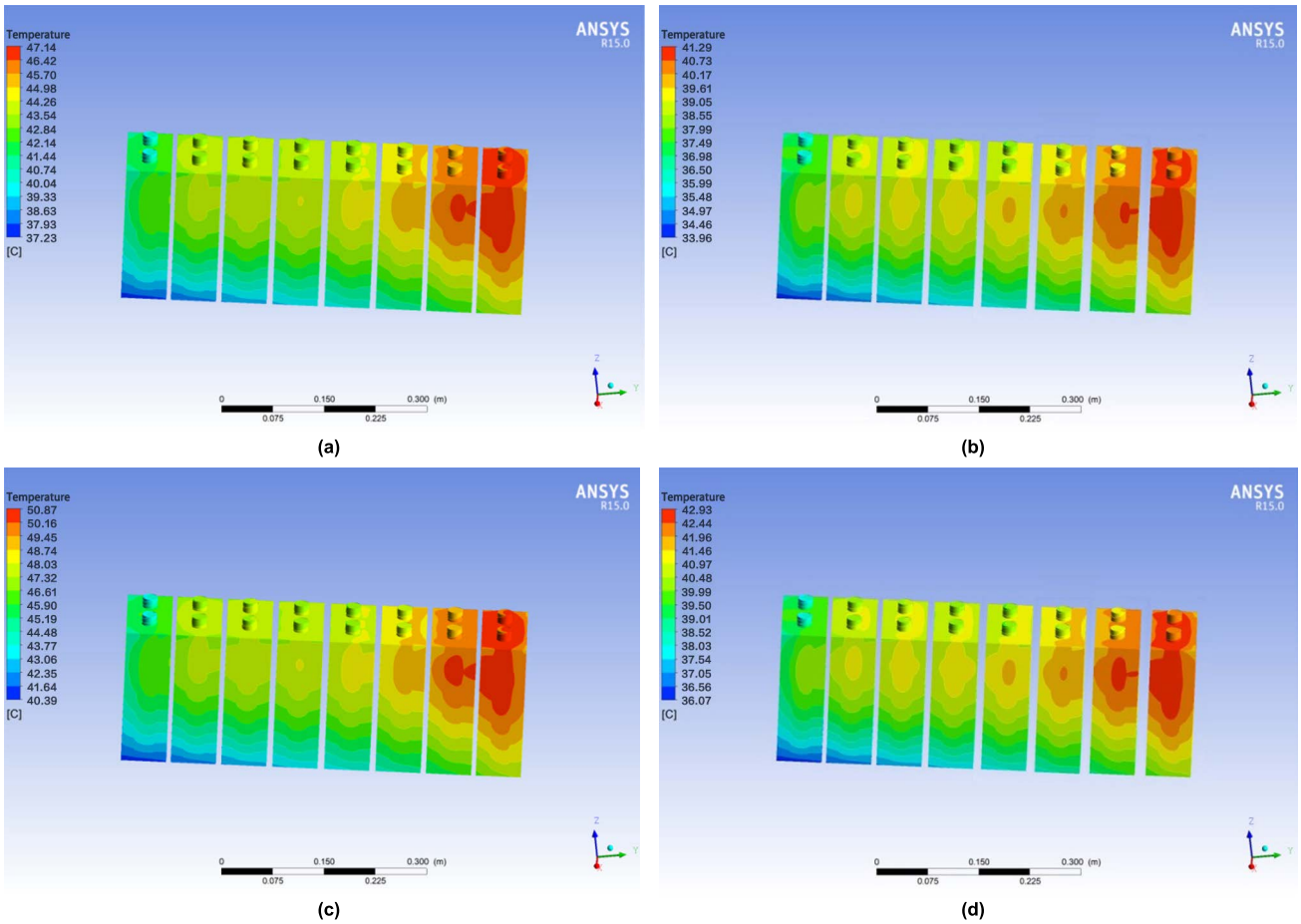

FIGURE 17. Temperature distribution before and after structural optimization under different ambient temperatures. (a) Initial structure under ambient temperature of 30 °C. (b) Optimized structure under ambient temperature of 30 °C. (c) Initial structure under ambient temperature of 35 °C. (d) Optimized structure under ambient temperature of 35 °C.

generalization ability corresponding to different batteries is not strong. The multi-objective optimization algorithm based on orthogonal experiment is to find the corresponding relationship between different parameters and heat dissipation performance after determining the initial structural parameters, and then optimize the structure by finding the optimal structural parameters through the method of orthogonal experiment. It is a commonly used optimization method at present. The structure optimized by this method has better heat dissipation performance, but the calculation amount is large and the process is more complicated. Algorithm-based optimization methods that utilize different algorithms and their variants or combinations (such as BPNN combined with GA or Gaussian process regression combined with non-dominated sorting genetic algorithm II) to optimize the relevant parameters through the mapping relationship between each parameter and the heat dissipation performance [31]. It is also a popular optimization method in various fields, and relies on machine learning, with low computational cost and good reliability, thus, it may be the trend for future research.

VI. CONCLUSION

An appropriate temperature range of the operating battery pack must be maintained and the temperature difference between the cells must be limited to ensure the safety of the EVs and optimize the charge and discharge performance of the battery. In this paper, the thermodynamic analysis of a pure EV lithium-ion battery is conducted to assess the effect of the temperature field distribution under different conditions. The reliability of the method is shown through the establishment of a numerical model and the thermodynamic analysis of the battery cell. The maximum heat generation rate ($24000 W/m^3$) is extracted through dynamic simulation by ADVISOR, which illustrates the higher requirements of the battery dissipation structure under the extra urban condition and driving at high speed. The structure of the heat dissipation of the battery pack is optimized based on BPNN-GA and the orthogonal experiment. Additionally, the optimal parameters for the proposed structure are as follows: 6.58 m/s (air flow rate), 1.0mm (spacing tolerance value) and 6.5°C (inlet angle). After optimization, the maximum temperature decreases from 45.04 °C to 40.86 °C (9.2% decrease),

while the maximum temperature decreases from 10.39 °C to 7.68 °C (26.1% decrease). Besides, the results of setting different ambient temperatures reveal that the proposed optimized structure reduces the temperature of the battery pack while effectively improving its heat dissipation performance.

ACKNOWLEDGMENT

The experimental equipment was supported by the National Engineering Laboratory for Highway Maintenance Equipment, Chang'an University, Xi'an, China.

REFERENCES

[1] R. Xiong, "Low-temperature heating and optimal charging methods for lithium-ion batteries," in *Battery Management Algorithm for Electric Vehicles*. Singapore: Springer, 2020, pp. 243–270.
[2] K. Chen, Y. Chen, Y. She, M. Song, S. Wang, and L. Chen, "Construction of effective symmetrical air-cooled system for battery thermal management," *Appl. Thermal Eng.*, vol. 166, Feb. 2020, Art. no. 114679.
[3] L. Ianniciello, P. H. Biwolé, and P. Achard, "Electric vehicles batteries thermal management systems employing phase change materials," *J. Power Sources*, vol. 378, pp. 383–403, Feb. 2018.
[4] D. W. Sundin and S. Sponholtz, "Thermal management of Li-ion batteries with single-phase liquid immersion cooling," *IEEE Open J. Veh. Technol.*, vol. 1, pp. 82–92, 2020, doi: 10.1109/OJVT.2020.2972541.
[5] H. Fathabadi, "High thermal performance lithium-ion battery pack including hybrid active–passive thermal management system for using in hybrid/electric vehicles," *Energy*, vol. 70, pp. 529–538, Jun. 2014.
[6] M. A. Hannan, M. S. H. Lipu, A. Hussain, M. H. Saad, and A. Ayob, "Neural network approach for estimating state of charge of lithium-ion battery using backtracking search algorithm," *IEEE Access*, vol. 6, pp. 10069–10079, 2018.
[7] X. Hu, H. Yuan, C. Zou, Z. Li, and L. Zhang, "Co-estimation of state of charge and state of health for lithium-ion batteries based on fractional-order calculus," *IEEE Trans. Veh. Technol.*, vol. 67, no. 11, pp. 10319–10329, Nov. 2018, doi: 10.1109/TVT.2018.2865664.
[8] C. She, L. Zhang, Z. Wang, F. Sun, P. Liu, and C. Song, "Battery state of health estimation based on incremental capacity analysis method: Synthesizing from cell-level test to real-world application," *IEEE J. Emerg. Sel. Topics Power Electron.*, early access, Sep. 14, 2021, doi: 10.1109/JESTPE.2021.3112754.
[9] Z. Wang, C. Song, L. Zhang, Y. Zhao, P. Liu, and D. G. Dorrell, "A data-driven method for battery charging capacity abnormality diagnosis in electric vehicle applications," *IEEE Trans. Transport. Electrific.*, vol. 8, no. 1, pp. 990–999, Mar. 2022, doi: 10.1109/TTE.2021.3117841.
[10] Y. Lai, W. Wu, K. Chen, S. Wang, and C. Xin, "A compact and lightweight liquid-cooled thermal management solution for cylindrical lithium-ion power battery pack," *Int. J. Heat Mass Transf.*, vol. 144, Dec. 2019, Art. no. 118581.
[11] M. Kiani, M. Ansari, A. A. Arshadi, E. Houshfar, and M. Ashjaee, "Hybrid thermal management of Lithium-ion batteries using nanofluids metal foam, and phase change material: An integrated numerical–experimental approach," *J. Thermal Anal. Calorimetry*, vol. 141, pp. 1703–1715, Feb. 2020.
[12] H. Jouhara, N. Serey, N. Khordehgah, R. Bennett, S. Almahmoud, and S. P. Lester, "Investigation, development and experimental analyses of a heat pipe based battery thermal management system," *Int. J. Thermofluids*, vols. 1–2, Feb. 2020, Art. no. 100004.
[13] Y. Huo, Z. Rao, X. Liu, and J. Zhao, "Investigation of power battery thermal management by using mini-channel cold plate," *Energy Convers. Manage.*, vol. 89, pp. 387–395, Jan. 2015.
[14] Y. S. Choi and D. M. Kang, "Prediction of thermal behaviors of an air-cooled lithium-ion battery system for hybrid electric vehicles," *J. Power Sources*, vol. 270, pp. 273–280, Dec. 2014.
[15] J. Smith, M. Hinterberger, P. Hable, and J. Koehler, "Simulative method for determining the optimal operating conditions for a cooling plate for lithium-ion battery cell modules," *J. Power Sources*, vol. 267, pp. 784–792, Dec. 2014.
[16] J. Soparat, W. Sritham, A. Teralapsuwan, C. Srisurangkul, and C.-N. Benyajat, "Computational study on design of battery cooling system for retrofitted EV passenger cars," SAE Technical Paper 2015-01-0102, 2015.
[17] Z. G. Yang, S. Huang, and L. P. Zhao, "Optimization design on heat dissipation of lithium-ion battery pack in electric vehicle," *Numer. Simul. Eng. CAE Algorithm*, vol. 20, no. 3, pp. 1–5, 2011.
[18] W. Tao, K. J. Tseng, J. Zhao, and Z. Wei, "Thermal investigation of lithium-ion battery module with different cell arrangement structures and forced air-cooling strategies," *Appl. Energy*, vol. 134, pp. 229–238, Dec. 2014.
[19] R. Mahamud and C. Park, "Reciprocating air flow for Li-ion battery thermal management to improve temperature uniformity," *J. Power Sources*, vol. 196, no. 13, pp. 5685–5696, Jul. 2011.
[20] S. K. Mohammadian, S. M. Rassoulinejad-Mousavi, and Y. Zhang, "Thermal management improvement of an air-cooled high-power lithium-ion battery by embedding metal foam," *J. Power Sources*, vol. 296, pp. 305–313, Nov. 2015.
[21] A. Jarrett and I. Y. Kim, "Design optimization of electric vehicle battery cooling plates for thermal performance," *J. Power Sources*, vol. 196, no. 23, pp. 10359–10368, Dec. 2011.
[22] J. Xie, Z. Ge, M. Zang, and S. Wang, "Structural optimization of lithium-ion battery pack with forced air cooling system," *Appl. Thermal Eng.*, vol. 126, pp. 583–593, Nov. 2017, doi: 10.1016/j.applthermaleng.2017.07.143.
[23] P. Nelson, D. Dees, K. Amine, and G. Henriksen, "Modeling thermal management of lithium-ion PNGV batteries," *J. Power Sources*, vol. 110, no. 2, pp. 349–356, Aug. 2002.
[24] X. Zhang, W. Wang, H. He, L. Hua, and J. Heng, "Optimization of the air-cooled supercapacitor module compartment for an electric bus," *Appl. Thermal Eng.*, vol. 112, pp. 1297–1304, Feb. 2017.
[25] D. Bernardi, E. Pawlikowski, and J. Newman, "A general energy balance for battery systems," *J. Electrochem. Soc.*, vol. 132, no. 1, pp. 5–12, Jan. 1985.
[26] Y. Wang, C. Zhang, Z. Chen, J. Xie, and X. Zhang, "A novel active equalization method for lithium-ion batteries in electric vehicles," *Appl. Energy*, vol. 145, pp. 36–42, May 2015.
[27] W. Wenwei, L. Cheng, T. Peng, and Z. Chengjun, "Thermal characteristic analysis of power lithium-ion battery system for electric vehicle," in *Proc. 3rd Int. Conf. Digit. Manuf. Autom.*, Jul. 2012, pp. 967–971.
[28] Y. Chen and U. Gross, "Estimation of thermal properties based on inverse heat conduction method," *J. Chem. Ind.*, vol. 56, no. 12, pp. 2415–2420, 2005.
[29] Z. T. Yu and C. Ji, "Research on the thermal characteristics of lithium-ion phosphate battery pack for electric vehicle," *Mach. Des. Manuf. Eng.*, vol. 45, no. 12, pp. 87–90, 2016.
[30] R. Xiong, F. Sun, X. Gong, and C. Gao, "A data-driven based adaptive state of charge estimator of lithium-ion polymer battery used in electric vehicles," *Appl. Energy*, vol. 113, pp. 1421–1433, Jan. 2014.
[31] Z. Xu, J. Xu, Z. Guo, H. Wang, Z. Sun, and X. Mei, "Design and optimization of a novel microchannel battery thermal management system based on digital twin," *Energies*, vol. 15, no. 4, p. 1421, Feb. 2022, doi: 10.3390/en15041421.
[32] P. Sun, Z. Gong, and Z. Chen, "Thermal optimization of lithium-ion battery modules based on PCM under extreme cycle operation," in *Proc. 12th Int. Conf. Intell. Comput. Technol. Autom. (ICICTA)*, Oct. 2019, pp. 724–729, doi: 10.1109/ICICTA49267.2019.00158.
[33] H. Nielsen, "Theory of the backpropagation neural network," in *Proc. Int. Joint Conf. Neural Netw.* Washington, DC, USA: IEEE Press, 1989, pp. 593–605.
[34] N. Wang, X. Zhu, and J. Zhang, "License plate segmentation and recognition of Chinese vehicle based on BPNN," in *Proc. 12th Int. Conf. Comput. Intell. Secur. (CIS)*, Dec. 2016, pp. 403–406, doi: 10.1109/CIS.2016.0098.
[35] W. Jiao and C. Ma, "Track prediction algorithm based on GA-BPNN," in *Proc. IEEE 3rd Int. Conf. Civil Aviation Saf. Inf. Technol. (ICCASIT)*, Oct. 2021, pp. 211–217, doi: 10.1109/ICCASIT53235.2021.9633519.
[36] S. Zhang, F. Wang, H. Fang, and Y. Yuan, "BPNN-GA-based intelligence information approach to characterize deep fractured strata," in *Proc. 6th Int. Conf. Inf. Sci. Control Eng. (ICISCE)*, Dec. 2019, pp. 185–189, doi: 10.1109/ICISCE48695.2019.00045.
[37] A. Sateria, B. O. P. Soepangkat, and R. Norcahyo, "Multi-objective optimization in drilling GFRP composite-stainless steel stacks using BPNN-GA method," in *Proc. Int. Conf. Appl. Sci. Technol. (iCAST)*, Oct. 2018, pp. 220–225, doi: 10.1109/iCAST1.2018.8751590.

YAN LI received the B.E. degree in mechanical design and manufacture and automation from the Xi'an University of Architecture and Technology, Xi'an, China, in 2020. He is currently pursuing the Ph.D. degree in mechanical engineering with the National Engineering Laboratory for Highway Maintenance Equipment, Chang'an University, Xi'an. His research interest includes battery thermal management systems.

HONGHAI LIU received the B.Sc. and M.Sc. degrees in mechanical engineering from Chang'an University, and the Ph.D. degree from the Wuhan University of Technology. He is currently working as a Full Professor with the School of Construction Machinery, Chang'an University. His research interests include intelligent technology of construction machinery, quality control of construction machinery operations, and highway maintenance technology and equipment.

MIN YE (Member, IEEE) received the B.Sc. and M.Sc. degrees in mechatronics engineering from Chang'an University, in 2000 and 2004, respectively, and the Ph.D. degree in mechatronics engineering from Xi'an Jiaotong University, in 2008. From 2008 to 2010, he was a Postdoctoral Researcher with Sany Heavy Industry Company. In 2013, he was a Visiting Scholar with the University of Michigan–Dearborn. Since 2015, he has been a Full Professor and the Vice Dean of the School of Construction Machinery, Chang'an University. His research interests include energy saving technology, hybrid power technology, and computational fluid mechanic.